1. THE MOMENT-BASED LOW-ORDER EQUATIONS

The formulation of the LO equations is similar to a discontinuous FE method. Weighted integrals of the the equations are taken with functions that have local support as weight functions. The equations are written with element-wise moments of I and T as unknowns. Leaving the solution in this form allows for use of information form a previous HO solution to eliminate auxillary unknowns from the equations. This is different than a standard Galerkin FE method [?] where a functional form of the solution is directly assumed. The final equations will have a similar form to S_2 equations, but we have not used a collocation method in angle, which should limit ray effects [?] in higher spatial dimensions. The equations eliminate extra spatial unknowns in a manner similar to to a linear-discontinuous FE method [?]. We also explore the possibility of using the MC solution to modify the discretization of the LO solution in Sec. ??. MOVE

The remainder of this chapter is structured as follows: the general moments will be derived and then the angular and spatial closure are discussed REWRITE. For simplicity, the backward Euler time discretization is used throughout this section. Sec. ?? will use the HO solution and MC transport to consistently close the equations in time, improving time accuracy.

1.1 Forming the Space-Angle Moment Equations

1.1.1 LO Spatial mesh and Finite-Element Spatial Moments

The LO equations are formulated over a FE mesh. The domain for the i-th spatial element (or cell) has support $x \in [x_{i-1/2}, x_{i+1/2}]$ with width $h_i = x_{i+1/2} - x_{i-1/2}$ and cell center $x_i = x_{i-1/2} + h_i/2$. There is a total of N_c elements, spanning the spatial domain $0 \leq x \leq X$. For simplicity, this spatial mesh is fixed throughout the

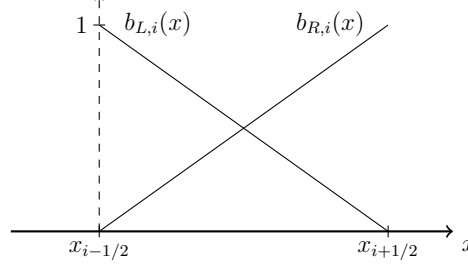simulation. Mesh adaptation is only applied in the HO solver.

Figure 1.1: Illustration of linear finite element basis functions $b_{L,i}(x)$ and $b_{R,i}(x)$ for spatial element i.

The spatial moments are defined by integrals weighted with the standard linear finite element (FE) interpolatory basis functions. An illustration of the two linear FE basis functions for the i-th element is given in Fig. 1.1. The left basis function is defined as

$$b_{L,i}(x) = \begin{cases} \frac{x_{i+1/2}-x}{h_i} & x_{i-1/2} \leq x \leq x_{i+1/2} \\ 0 & \text{elsewhere} \end{cases}, \qquad (1.1)$$

corresponding to the node $x_{i-1/2}$. The right basis function is

$$b_{R,i}(x) = \begin{cases} \frac{x-x_{i-1/2}}{h_i} & x_{i-1/2} \leq x \leq x_{i+1/2} \\ 0 & \text{elsewhere} \end{cases}, \qquad (1.2)$$

corresponding to the node $x_{i+1/2}$. With these definitions, a local linear approximation to a function f can be formulated as $f(x) \simeq f_{L,i}b_{L,i}(x) + f_{R,i}b_{R,i}(x), \quad x \in [x_{i-1/2}, x_{i+1/2}]$.[1]

---

[1]In literature the FE functions are formally defined with support over two adjacent elements. However, in our notation our functions only have non-zero support in element i. This accommodates our later definition of moments and discontinuous unknowns.

The spatial moments are defined by integrals over the each element, using the two basis functions. We use $\langle \cdot \rangle$ to indicate integration over a spatial element. The spatial moments are

$$\langle \cdot \rangle_{L,i} = \frac{2}{h_i} \int_{x_{i-1/2}}^{x_{i+1/2}} b_{L,i}(x)(\cdot)\mathrm{d}x \tag{1.3}$$

and

$$\langle \cdot \rangle_{R,i} = \frac{2}{h_i} \int_{x_{i-1/2}}^{x_{i+1/2}} b_{R,i}(x)(\cdot)\mathrm{d}x. \tag{1.4}$$

where the factor of $2/h_i$ is a normalization constant. It is noted in this notation $\langle \phi \rangle_{L,i}$ and $\langle \phi \rangle_{R,i}$ represent spatial moments of the intensity over cell i, opposed to $\phi_{L,i}$ and $\phi_{R,i}$, which represent the interior value of the linear representation of $\phi(x)$ at $x_{i-1/2}$ and $x_{i+1/2}$ within the cell.

To simplify notation and discussion, we also define the slope and average moments over a spatial cell. The average scalar intensity is

$$\phi_i = \frac{1}{h_i} \int_{x_{i-1/2}}^{x_{i+1/2}} \phi(x)\mathrm{d}x \tag{1.5}$$

and

$$\phi_{x,i} = \frac{6}{h_i} \int_{x_{i-1/2}}^{x_{i+1/2}} \left(\frac{x - x_i}{h_i} \right) \phi(x)\mathrm{d}x. \tag{1.6}$$

The linear representation over a cell in terms of these moments is $\phi(x) = \phi_i + 2\phi_{x,i}(x - x_i)/h_i^2$, for $x \in (x_{i-1/2}, x_{i+1/2})$.

1.1.2 Definition of Angular Moments

To reduce the angular dimensionality, positive and negative half-range integrals of the angular intensity are taken. The angular integrals are denoted with a superscript as

$$(\cdot)^\pm = \pm \int_0^{\pm 1} (\cdot)\mathrm{d}\mu \tag{1.7}$$

3

The half-range integrals of I are defined as $\phi^+(x,t) = \int_0^1 I(x,\mu,t)\,\mathrm{d}\mu$ and $\phi^-(x,t) = 2\pi \int_{-1}^0 I(x,\mu,t)\,\mathrm{d}\mu$, respectively. Thus, in terms of half-range quantities, the mean intensity is $\phi = \phi^- + \phi^+$. It is noted that in this notation the flux is defined as $J = J^- + J^+$, which is not the standard definition for the half-range fluxes, e.g., in [2].

1.1.3 Space-Angle Moments of the Radiation Transport Equation

The LO radiation equations are formed by applying the space and angle moment operators to the transport equation and performing algebraic manipulation. We provide a detailed derivation of the L and $+$ radiation moment equation and state the final results for the other moment operators. First, the L moment operator is applied to the time-discretized transport equation, i.e., Eq. (??). Integration by parts on the streaming term yields

$$-\frac{2}{h_i}\mu_{i-1/2}I_{i-1/2}^{n+1} + \frac{2}{h_i^2}\int_{x_{i-1/2}}^{x_{i+1/2}} \mu I^{n+1}\mathrm{d}x + \left(\sigma_{t,i}^{n+1} + \frac{1}{c\Delta t}\right)\langle\phi\rangle_{L,i}^{n+1,+}$$
$$-\frac{\sigma_{s,i}}{2}\langle\phi\rangle_{L,i}^{n+1} = \frac{1}{2}\langle\sigma_a^{n+1}acT^{n+1,4}\rangle_{L,i} + \frac{1}{c\Delta t}\langle\phi\rangle_{L,i}^{n,+}. \quad (1.8)$$

Here, the cross sections have been assumed constant over a cell. The mean intensity in the scattering term is expanded in terms of half-range unknowns. The integral can be rewritten in terms of L and R moments by noting that $b_{L,i}(x)+b_{R,i}(x) = 2/h_i$. These substitutions are made and the resulting equation is multiplied by h_i to produce

$$-2\mu_{i-1/2}I_{i-1/2}^{n+1} + \langle\mu I^{n+1}\rangle_{L,i} + \langle\mu I^{n+1}\rangle_{R,i} + \left(\sigma_{t,i}^{n+1} + \frac{1}{c\Delta t}\right)h_i\langle\phi\rangle_{L,i}^{n+1,+}$$
$$-\frac{\sigma_{s,i}h_i}{2}\left(\langle\phi\rangle_{L,i}^{n+1,+} + \langle\phi\rangle_{L,i}^{n+1,-}\right) = \frac{h_i}{2}\langle\sigma_a^{n+1}acT^{n+1,4}\rangle_{L,i} + \frac{h_i}{c\Delta t}\langle\phi\rangle_{L,i}^{n,+}. \quad (1.9)$$

The resulting equation is integrated over the positive half range:

$$-2\left(\mu_{i-1/2}I_{i-1/2}^{n+1}\right)^+ + \langle\mu I^{n+1}\rangle_{L,i}^+ + \langle\mu I^{n+1}\rangle_{R,i}^+ + \left(\sigma_{t,i}^{n+1} + \frac{1}{c\Delta t}\right)h_i\langle\phi\rangle_{L,i}^{n+1,+}$$

$$-\frac{\sigma_{s,i}h_i}{2}\left(\langle\phi\rangle_{L,i}^{n+1,+} + \langle\phi\rangle_{L,i}^{n+1,-}\right) = \frac{h_i}{2}\langle\sigma_a^{n+1}acT^{n+1,4}\rangle_{L,i} + \frac{h_i}{c\Delta t}\langle\phi\rangle_{L,i}^{n,+}. \quad (1.10)$$

1.1.4 The Angular Consistency Terms

Now, algebraic manipulations are performed on the streaming terms to produce face and volume-averaged values of μ, weighted by the intensity. Each term in the streaming term is multiplied by a factor of unity, with the desired unknown appropriate to each term in the numerator and denominator. Temporarily dropping the time index for clarity, the manipulations applied to the streaming term are as follows:

$$\left\langle\mu\frac{\partial I}{\partial x}\right\rangle_L^+ = -\frac{2}{h_i}\left(\mu I_{i-1/2}\right)^+ + \frac{1}{h_i}\left[\langle\mu I\rangle_{L,i}^+ + \langle\mu I\rangle_{R,i}^+\right] \quad (1.11)$$

$$= -\frac{2}{h_i}\left(\mu I_{i-1/2}\right)^+\frac{(I_{i-1/2})^+}{(I_{i-1/2})^+} + \frac{1}{h_i}\left[\langle\mu I\rangle_{L,i}^+\frac{\langle I\rangle_{L,i}^+}{\langle I\rangle_{L,i}^+} + \langle\mu I\rangle_{R,i}^+\frac{\langle I\rangle_{R,i}^+}{\langle I\rangle_{R,i}^+}\right] \quad (1.12)$$

$$= -\frac{2}{h_i}\left\{\frac{(\mu I)_{i-1/2}^+}{\phi_{i-1/2}^+}\right\}\phi_{i-1/2}^+ + \frac{1}{h_i}\left[\left\{\frac{\langle\mu I\rangle_{L,i}^+}{\langle\phi\rangle_{L,i}^+}\right\}\langle\phi\rangle_{L,i}^+ + \left\{\frac{\langle\mu I\rangle_{R,i}^+}{\langle\phi\rangle_{R,i}^+}\right\}\langle\phi\rangle_{R,i}^+\right]$$

$$(1.13)$$

The ratios in braces are what we will formally define as *angular consistency terms*. These nonlinear functionals are approximated by the HO solver. The angular consistency term for the L and $+$ moments is defined as

$$\{\mu\}_{L,i}^{n+1,+} \equiv \frac{\langle\mu I^{n+1}\rangle_{L,i}^+}{\langle I^{n+1}\rangle_{L,i}^+} = \frac{\dfrac{2}{h_i}\displaystyle\int_0^1\int_{x_{i-1/2}}^{x_{i+1/2}}\mu\,b_{L,i}(x)I^{n+1}(x,\mu)\mathrm{d}x\mathrm{d}\mu}{\dfrac{2}{h_i}\displaystyle\int_0^1\int_{x_{i-1/2}}^{x_{i+1/2}}b_{L,i}(x)I^{n+1}(x,\mu)\mathrm{d}x\mathrm{d}\mu}. \quad (1.14)$$

5

The consistency terms on the face represent averaging at a point, with a similar definition as

$$\mu_{i+1/2}^{+} \equiv \frac{\left(\mu I_{i+1/2}\right)^{+}}{\phi_{i+1/2}^{+}} = \frac{\displaystyle\int_{0}^{1} \mu I(x_{i+1/2}, \mu) \mathrm{d}\mu}{\displaystyle\int_{0}^{1} I(x_{i+1/2}, \mu) \mathrm{d}\mu} \ . \tag{1.15}$$

There are analogous definitions for the R and $-$ moments. The moment of the streaming term for the L and $+$ operators becomes

$$\left\langle \mu \frac{\partial I}{\partial x} \right\rangle_{L}^{+} = -\frac{2}{h_i} \mu_{i-1/2}^{+} I_{i-1/2}^{+} + \frac{1}{h_i} \left[\{\mu\}_{L,i}^{+} \langle\phi\rangle_{L,i}^{+} + \{\mu\}_{R,i}^{+} \langle\phi\rangle_{R,i}^{+} \right] \tag{1.16}$$

It is noted that this expression does not contain a cross section in the denomainator, such as in the variable Eddington factor approach [?], thus this method will be stable in a void.

1.1.5 The Exact Radiation Moment Equations

A final expression for the moment equation resulting from application of the L moment and positive half-range integral is obtained by substituting the result of Eq. (1.16) into Eq. (1.10):

$$-2\mu_{i-1/2}^{n+1,+} \phi_{i-1/2}^{n+1,+} + \{\mu\}_{L,i}^{n+1,+} \langle\phi\rangle_{L,i}^{n+1,+} + \{\mu\}_{R,i}^{n+1,+} \langle\phi\rangle_{R,i}^{n+1,+} + \left(\sigma_{t,i}^{n+1} + \frac{1}{c\Delta t} \right) h_i \langle\phi\rangle_{L,i}^{n+1,+}$$

$$- \frac{\sigma_{s,i} h_i}{2} \left(\langle\phi\rangle_{L,i}^{n+1,+} + \langle\phi\rangle_{L,i}^{n+1,-} \right) = \frac{h_i}{2} \langle\sigma_a^{n+1} acT^{n+1,4}\rangle_{L,i} + \frac{h_i}{c\Delta t} \langle\phi\rangle_{L,i}^{n,+}, \quad (1.17)$$

Similar derivations can be used to derive the other radiation moment equations. Pairwise application of the L and R basis moments with the $+$ and $-$ half-range integrals to Eq. (??) ultimately yields four moment equations per cell. The equation

6

for the R and $+$ moment is

$$2\mu_{i+1/2}^{n+1,+}\phi_{i+1/2}^{n+1,+} - \{\mu\}_{L,i}^{n+1,+}\langle\phi\rangle_{L,i}^{n+1,+} - \{\mu\}_{R,i}^{n+1,+}\langle\phi\rangle_{R,i}^{n+1,+} + \left(\sigma_{t,i}^{n+1} + \frac{1}{c\Delta t}\right)h_i\langle\phi\rangle_{R,i}^{n+1,+}$$

$$- \frac{\sigma_{s,i}h_i}{2}\left(\langle\phi\rangle_{R,i}^{n+1,+} + \langle\phi\rangle_{R,i}^{n+1,-}\right) = \frac{h_i}{2}\langle\sigma_a^{n+1}acT^{n+1,4}\rangle_{R,i} + \frac{h_i}{c\Delta t}\langle\phi\rangle_{R,i}^{n,+}, \quad (1.18)$$

The equations for the negative half-range moment are identical to the above with the negative half-range superscripts replacing the positive. Explicitly,

$$-2\mu_{i-1/2}^{n+1,-}\phi_{i-1/2}^{n+1,-} + \{\mu\}_{L,i}^{n+1,-}\langle\phi\rangle_{L,i}^{n+1,-} + \{\mu\}_{R,i}^{n+1,-}\langle\phi\rangle_{R,i}^{n+1,-} + \left(\sigma_{t,i}^{n+1} + \frac{1}{c\Delta t}\right)h_i\langle\phi\rangle_{L,i}^{n+1,-}$$

$$- \frac{\sigma_{s,i}h_i}{2}\left(\langle\phi\rangle_{L,i}^{n+1,+} + \langle\phi\rangle_{L,i}^{n+1,-}\right) = \frac{h_i}{2}\langle\sigma_a^{n+1}acT^{n+1,4}\rangle_{L,i} + \frac{h_i}{c\Delta t}\langle\phi\rangle_{L,i}^{n,-} \quad (1.19)$$

and

$$2\mu_{i+1/2}^{n+1,-}\phi_{i+1/2}^{n+1,-} - \{\mu\}_{L,i}^{n+1,-}\langle\phi\rangle_{L,i}^{n+1,-} - \{\mu\}_{R,i}^{n+1,-}\langle\phi\rangle_{R,i}^{n+1,-} + \left(\sigma_{t,i}^{n+1} + \frac{1}{c\Delta t}\right)h_i\langle\phi\rangle_{R,i}^{n+1,-}$$

$$- \frac{\sigma_{s,i}h_i}{2}\left(\langle\phi\rangle_{R,i}^{n+1,+} + \langle\phi\rangle_{R,i}^{n+1,-}\right) = \frac{h_i}{2}\langle\sigma_a^{n+1}acT^{n+1,4}\rangle_{R,i} + \frac{h_i}{c\Delta t}\langle\phi\rangle_{R,i}^{n,-}, \quad (1.20)$$

Ultimately, the two half-ranges will be treated differently when the equations are closed spatially.

1.1.6 Material Energy Equations

To derive the LO material energy equations, an approximation must be introduced to relate $T(x)$ and $T^4(x)$ within a cell. We represent $T(x)$ spatially with a LDFE trial space. This trial space will ensure preservation of the equilibrium diffusion limit. To simplify the relation between $T(x)$ and $T^4(x)$ $T(x) \simeq T_{L,i}b_{L,i}(x) + T_{R,i}b_{R,i}(x)$, $x \in (x_{i-1/2}, x_{i+1/2})$. Similarly, the emission term is represented in the material and radiation equations with the LDFE interpolant $T^4(x) \simeq T_{L,i}^4 b_{L,i}(x) +$

$T_{R,i}^4 b_{R,i}(x)$. The L and R spatial moments are taken of the material energy equations; the LDFE representations for $T(x)$ and $\sigma_a ac T^4(x)$ are used to simplify the spatial integrals. The final LO material energy equation resulting from application of the L moment is

$$\frac{\rho_i c_{v,i}}{\Delta t} \left[\left(\frac{2}{3}T_{L,i} + \frac{1}{3}T_{R,i}\right)^{n+1} - \left(\frac{2}{3}T_{L,i} + \frac{1}{3}T_{R,i}\right)^n \right] + \sigma_{a,i}^{n+1} \left(\langle\phi\rangle_{L,i}^+ + \langle\phi\rangle_{L,i}^-\right)^{n+1}$$
$$= \sigma_{a,i}^{n+1} ac \left(\frac{2}{3}T_{L,i}^4 + \frac{1}{3}T_{R,i}^4\right)^{n+1}. \quad (1.21)$$

The equation for the R moment is

$$\frac{\rho_i c_{v,i}}{\Delta t} \left[\left(\frac{1}{3}T_{L,i} + \frac{2}{3}T_{R,i}\right)^{n+1} - \left(\frac{1}{3}T_{L,i} + \frac{2}{3}T_{R,i}\right)^n \right] + \sigma_{a,i}^{n+1} \left(\langle\phi\rangle_{R,i}^+ + \langle\phi\rangle_{R,i}^-\right)^{n+1}$$
$$= \sigma_{a,i}^{n+1} ac \left(\frac{1}{3}T_{L,i}^4 + \frac{2}{3}T_{R,i}^4\right)^{n+1}. \quad (1.22)$$

Cross sections have been assumed constant over each element, evaluated at the average temperature within the element, i.e., $\sigma_{a,i}^{n+1} = \sigma_{a,i}([T_{L,i}^{n+1} + T_{R,i}^{n+1}]/2)$. Because the material energy balance only contains angularly integrated quantities, there is no need to take angular moments of the above equations.

REWRITE: WHAT TO DO WITH THIS PARAGRAPH? Because there are no derivatives of T in Eq. (??), there is no need to define T on the faces. Because only moments of ϕ appear in the material energy equations, they are fully defined at this point. The LD closure for the L and $+$ equations produces

1.2 Closing the LO System with Information from the HO Solution

The six degrees of freedom (DOF) over each cell i are the four moments $\langle\phi\rangle_{L,i}^+$, $\langle\phi\rangle_{R,i}^+$, $\langle\phi\rangle_{L,i}^-$, and $\langle\phi\rangle_{R,i}^-$ and the two spatial edge values $T_{L,i}$ and $T_{R,i}$. The four

radiation and two material energy equations define a system of equations for the six DOF, coupled spatially through the streaming term. We emphasize that at this point we have not made any spatial or angular approximations to the transport moment equations; these moment equations are exact with respect to the chosen time discretization. The material energy equation has the approximation of an LDFE space for $T(x)$. Some approximation of this form is necessary to relate T and T^4.

1.2.1   Angular Closure

The angular consistency parameters (e.g., Eq. (1.14) and (1.15)) are not known a priori. A lagged estimate of I^{n+1} from the previous HO solve is used to estimate the angular consistency parameters. In the HOLO algorithm, the equations for LO unknowns at iteration $k+1$ use consistency parameters computed using the latest HO solution $\tilde{I}^{n+1,k+1/2}$ as an approximation for $I^{n+1}(x,\mu)$. We evaluate these terms using quadruature based on the functional form of the solution provided by the HO solution.

1.2.2   Spatial Closure

The relation between the volume and face averaged quantities must be known to eliminate the final auxillary unknowns. To close the LO system spatially, we will explore multiple options. The simplest closure is to use a linear-discontinuous (LD) spatial closure with the usual upwinding approximation [?]. For example, for positive flow (e.g., Eq. (??)) the face terms $\mu_{i-1/2}$ and $\phi_{i-1/2}$ are upwinded from the previous cell $i-1$ or from a boundary condition; the terms at $x_{i+1/2}$ are linearly extrapolated, computed using the L and R basis moments. By assuming $\phi^{\pm}(x)$ is linear over a cell, a relation between the outflow and moments can be derived, e.g., $\phi^{+}_{i+1/2} = 2\langle\phi\rangle^{+}_{R} - \langle\phi\rangle^{+}_{L}$. For the negative half range, $\phi^{-}_{i-1/2} = 2\langle\phi\rangle^{-}_{L} - \langle\phi_R\rangle^{+}$. The LD

closure, with upwinding, for the L equation and positive half-range is

$$-2\mu_{i-1/2}^{n+1,+}\left(2\langle\phi\rangle_{R,i-1}^{+}-\right)+\{\mu\}_{L,i}^{n+1,+}\langle\phi\rangle_{L,i}^{n+1,+}+\{\mu\}_{R,i}^{n+1,+}\langle\phi\rangle_{R,i}^{n+1,+}+\left(\sigma_{t,i}^{n+1}+\frac{1}{c\Delta t}\right)h_i\langle\phi\rangle_{L,i}^{n+1,+}-\frac{\sigma_{s,i}h_i}{2}\left(\langle\phi\rangle\right.$$

(1.23)

Similar equations can be derived for the other directions, fully defining the radiation equations. These equations are equivalent to an S_2

Note that we have chosen to leave $\mu_{i-1/2}^{n+1,+}$ as a value to be estimated from the HO solver, which is more conducive to the other spatial closures described in Sec. **??**. Alternatively, the spatial closure could be introduced before performing the algebraic manipulation to form consistency terms (e.g., into Eq. (1.11)). This would produce only volume-weighted consistency terms for the LD spatial closure.

1.2.2.1 Fixups to LD Solution

The linear-discontinuous (LD) closure with upwinding is not strictly positive. In particular, for optically thick cells with a steep intensity gradient, the solution becomes negative. These negative values of intensity can propagate to adjacent cells. In thick regions of TRT problems, reasonably fine spatial cells can still be on the order of millions of mean free paths; negative values with an LD representation are unavoidable in practice for such cells and mesh refinement is of minimal use. Typically, for a standard LDFE method, the equations are lumped to produce a strictly positive solution (for 1D) [**?**]. However, standard FE lumping procedures would introduce difficulties in computing the consistency terms from the HO solution. Thus, an alternative spatial closure is used that is equivalent to the standard FE lumping procedure. The L and R moments are defined the same as before, preserving the average within a cell, but the relation between the moments and the outflow is modified. For example, for positive μ, the outflow is now defined as $\phi_{i+1/2}^{+}=\langle\phi\rangle_R^{+}$.

Because the basis function $b_{R,i}(x)$ is strictly positive, the outflow is positive. This closure is only used in cells where negative intensities occur.

1.2.3 Newton's Method for LO Equations

Adding the equations for each cell together forms a global system of coupled equations. The equations are nonlinear due to the Planckian emission source. We have used Newton's method to solve the nonlinear system, based on a typical linearization of the Planckian source with cross sections evaluated at temperatures from the previous iteration, as described in [?]. A derivation of the LO Newton equations is given in ??.

The equations for each half-range are coupled together via scattering. In one spatial dimension, the scattering terms can be included in the discrete system matrix and directly inverted. We consider an alternative iterative solution method that could be more easily extended to higher spatial dimensions in Sec. ??. Isotropic scattering, including effective scattering terms from the linearization, are included in the system matrix. The system matrix is an asymmetric, banded matrix with a band width of seven and is inverted directly. Newton iterations are repeated until $\phi^{n+1}(x)$ and $T^{n+1}(x)$ are converged to a desired relative tolerance. Convergence is calculated using the spatial L_2 norm of the change in $\phi^{n+1}(x)$ and $T^{n+1}(x)$, relative to the norm of each solution. The lumping-equivalent discretization discussed above is used for cells where the solution for ϕ^{n+1} becomes negative. When negative values for $\phi^{n+1,\pm}(x)$ are detected, the lumping-equivalent discretization is used within those cells and that Newton step is repeated.

1.3 COMPUTATIONAL RESULTS

We will compare results of the HOLO method to IMC with a source tilting algorithm for two test problems [?]. Also, we briefly compare performance in Section 1.3.3. For all IMC results, no local, discrete diffusion acceleration methods for effective scattering (e.g., those in [?, ?]) are applied. Finally, we will demonstrate the efficiency advantage of ECMC in our HOLO algorithm by comparing the results to the same HOLO algorithm if the ECMC algorithm is replaced with a standard Monte Carlo (SMC) simulation. Results are also given for the case of a single ECMC batch, which is similar to a RMC method.

A measure of variance in cell-averaged scalar intensities was calculated to provide a quantitative measure of the statistical accuracy of different solution methods. To form sample standard deviations, twenty independent simulations for each particular result were performed using unique random number generator seeds. The variance of a particular cell-averaged $\phi(x)$ is

$$S_i^2 = \frac{20}{20-1} \sum_{l=1}^{20} \left(\overline{\phi}_i - \phi_i^l \right)^2, \tag{1.24}$$

where ϕ_i^l is the cell-averaged scalar intensity for cell i from the l-th of 20 independent simulations and $\overline{\phi}_i$ is the corresponding sample mean from the 20 simulations. To provide a normalized, spatially-integrated result, we form a norm over cells as

$$ß = \left(\frac{\sum\limits_{i=1}^{N_c} S_i^2}{\sum\limits_{i=1}^{N_c} \overline{\phi}_i^2} \right)^{1/2}, \tag{1.25}$$

where N_c is the number of spatial cells.

We will also form a figure of merit (FOM) to demonstrate how statistical accuracy scales with the number of histories performed. Our FOM is defined as

$$\text{FOM} = \frac{1}{N_{\text{tot}}ß^2} \tag{1.26}$$

where N_{tot} is the total number of histories performed over the simulation. A larger value of the FOM indicates that the method produced less variance in the solution per history performed, for a given problem. This form of the FOM is typically chosen because the variance is expected to reduce inversely proportional to N_{tot}, so for standard MC simulations the FOM becomes, on average, independent of N_{tot} [4]. The FOM is not necessarily expected to be independent of N_{tot} for IMC or our HOLO method due to correlation of the solution between time steps; additionally, ECMC has correlations between batches.

1.3.1   Marshak Wave

For the first problem, the radiation and material energies are initially in equilibrium at 2.5×10^{-5} keV. An isotropic incident intensity of 0.150 keV is applied at $x = 0$; the incident intensity on the right boundary is 2.5×10^{-5} keV. The material properties are $\rho = 1$ g cm^{-3} and $c_v = 0.013784$ jks/keV-g. The absorption cross section varies as $\sigma(T) = 0.001 \; \rho \; T^{-3}$ (cm^{-1}). The simulation was advanced until $t = 5$ sh (1 sh $\equiv 10^{-8}$ s) with a fixed time step size of 0.001 sh. For comparison purposes, we have not used adaptive mesh refinement, only performed one HOLO iteration per time step, and use a fixed 3 HO batches with equal number of histories per batch. A relative tolerance of 10^{-6} for the change in $\phi(x)$ and $T(x)$ was used for the LO newton solver for all results. Radiation energy distributions are plotted as an equivalent temperature given by $T_r = (\phi/(ac))^{0.25}$. Cell-averaged quantities are plotted. Although isotropic scattering is handled by the LO solver in the algorithm

13

described above, we have only considered problems with $\sigma_s = 0$ here. Results for neutronics with isotropic scattering included are given in [?].

Fig. 1.2a compares the cell-averaged radiation temperatures for the IMC and HOLO method with ECMC, for various number of spatial mesh cells N_c; we have used HOLO-ECMC to denote our algorithm because later results will use different HO solvers. For all IMC calculations, $n = 10^5$ histories per time step were used. For the HOLO method, we have used 4 equal-sized cells in μ for the finite-element angular mesh used by the ECMC solver. The spatial grid is the same for the HO and LO solvers. For the cases of $N_c = 25$ and $N_c = 200$, $4,000$ histories per batch ($n = 12,000$ per time step) were used. For $N_c = 500$, 16,000 histories per time step were used due to increased number of space-angle cells that need to be sampled. The IMC and HOLO solutions agree as the mesh is converged. There is similar agreement in the location of the wavefront due to the linear shape of the emission source over a cell. The cells nearest the wavefront required use of the lumping-equivalent discretization and S_2 equivalent terms during the LO solve, resulting in strictly positive solutions.

Fig. 1.2b compares solutions for the case of 200 cells. For the IMC solution 10^5 histories per time step were simulated; for the HOLO method only $4,000$ histories per batch (12,000 per time step) were simulated. There is significant statistical noise in the IMC solution compared to the HOLO solution. The HOLO solution visually demonstrates no statistical noise. Because the ECMC solve is only determining the change over the time step, the statistical noise in the result is small relative to the magnitude of I^{n+1}. Also, the source sampling only places particles in cells where the residual is large. No particles are sampled in the equilibrium region out front of the wave.

Table 2.1 compares ß and the FOM for IMC and the HOLO method, for different

14

numbers of histories per time step. The FOM results are normalized to the value for IMC with $n = 12,000$. The HOLO method demonstrates less variance for the same numbers of histories, producing FOM values that are two orders of magnitude greater than for IMC. Where as the FOM remains relatively constant for IMC, as n is increased the FOM improves for the HOLO method. This is a result of each batch producing more statistically accurate estimates of the error ϵ, which results in an increased convergence rate of ϵ overall.

Table 1.1: **Comparison of sample statistics for the Marshak Wave problem. Simulation end time is t = 5 sh.**

	ß		FOM	
hists./step	IMC	HOLO-ECMC	IMC	HOLO-ECMC
12,000	3.40%	0.28%	1	145
100,000	1.22%	0.057%	0.93	422

1.3.2   Two Material Problem

This problem consists of an optically thin (left) and an optically thick (right) material region, with temperature-independent cross sections. The material properties are given in Table 1.2. Initially the radiation and material energies are in equilibrium at a temperature of 0.05 keV. An isotropic incident intensity of 0.500 keV is applied at $x = 0$ at $t = 0$; the isotropic incident intensity on the right boundary is 0.05 keV. The simulation end time is 5 sh. For all HOLO simulations, we have used 8 equal-sized mesh cells in μ. As for the Marshak problem, the cells nearest the wavefront required use of the lumping-equivalent discretization and S_2 equivalent terms during the LO solve.

15

Table 1.2: Material properties for two material problem

	$x \in [0, 0.5)$ cm	$x \in [0.5, 1.0]$ cm
σ_a (cm^{-1})	0.2	2000
ρ (g cm^{-3})	0.01	10.0
c_v (jks/keV-g)	0.1	0.1

Fig. 1.3a compares the HOLO and IMC radiation temperatures at the end of the simulation. The IMC and HOLO results show good agreement over the finer mesh. On the coarse mesh ($N_c = 20$), the LDFE representation of T^4 in the HOLO method predicts the location of the wavefront more accurately than the IMC method with source tilting.

Fig. 1.3b demonstrates the benefit of ECMC as a HO solver compared to standard MC. The HOLO algorithm with the ECMC HO solver (HOLO-ECMC) results are for running 3 batches of 10,000 histories, per time step. The solution for the HOLO method with a standard MC solver as the HO solver (HOLO-SMC) with standard source sampling uses 10^5 histories per time step. The HOLO-SMC solution demonstrates significant statistical noise. This noise is introduced into the LO solver by bad statistics in computing the consistency terms. Also plotted is an S$_2$ solution obtained with consistency terms that are equivalent to S$_2$ and no HO correction. The S$_2$ solution results in an artificially fast wavefront, as expected, demonstrating the necessity of HO correction in this problem.

Table 1.3 compares the FOM and ß for IMC and the HOLO-ECMC method. The FOM values are normalized to the value for IMC with $n = 30,000$. The end time was reduced to 2 sh for these results to reduce computational times. The reduction in variance by the HOLO method over IMC is substantial. The improvement of the

FOM for the HOLO method compared to IMC is greater than for the Marshak wave problem. This improvement is because the wave moves much slower in right region of this problem, due to the large, constant cross section. Also, in the optically thin region of the problem the solution quickly comes to equilibrium. Thus, the ECMC algorithm has to estimate a very small change in the intensity over a time step. Additionally, difficulties in resolving the solution at the wavefront are not as severe compared to the Marshak wave problem, where the cold cells have a much larger cross section.

Table 1.3: **Comparison of sample statistics for the two material problem for 200 x cells. Simulation end time is t = 2 sh.**

	ß		s_{max}	
hists./step	IMC	HOLO-ECMC	IMC	HOLO-ECMC
30,000	3.63%	0.01%	1	104,000
100,000	1.96%	0.003%	1.03	360,000

1.3.3   Performance comparison of IMC and HOLO-ECMC

We have measured the total CPU time for simulations to provide a simplified measure of the computational cost. These results compare how computational times change the two different problems and how the methods scale with time step size and particle histories. Absolute comparisons in the computational cost of the two methods cannot be made because the methods are implemented in different code infrastructures. Additionally, the HOLO method fully resolves non-linearities at each time step, whereas IMC is using a single linearized step with lagged cross sections. Simulations were performed on the same processor, using a single CPU

core. Reported times are the average of 10 runs and all results used 200 x cells, $\Delta t = 0.001$ sh, and an end time of $t = 2$ sh.

Table 1.4 compares the average simulation time per history performed for the Marshak wave problem. The average time per history is computed by dividing the total simulation time by the total number of histories performed (e.g., the time of the LO solves is included for the HOLO method). Results are given for different numbers of histories per time step, as well as a case with an increased time step size. The table also includes the number of LO iterations performed per LO solve for the HOLO method, averaged over all time steps; there are two LO solves per time step. The same results are reported for the two material problem in Table 1.5.

The HOLO method does not scale with the number of histories due to the fixed cost of the LO solver. The cost of the LO solver is more significant at the lower history counts compared to the case of 10^5 histories, for both problems. There is a slight increase in the number of newton iterations as the time step is increased, but the average cost per history is not significantly increased. Similar to the results in [?], as the time step size is increased to to 0.005 sh, the IMC method increases in cost per time step, due to an increase in effective scattering events, particularly for the two material problem. Because the cross sections in the the two material problem do not have a T^{-3} behavior,the cost of the effective scattering cross section in IMC is more apparent, resulting in longer simulation times.

Table 1.4: **Comparison of average CPU times per history and LO iteration counts for the Marshak Wave problem.**

hists./step	$\Delta t(sh)$	IMC (μs/hist.)	HOLO-ECMC (μs/hist)	Newton iters./LO solve
100,000	0.001	10	5.3	3.8
12,000	0.001	9.7	8.1	4.1
12,000	0.005	19	9.4	6.2

Table 1.5: **Average CPU times per history and LO iteration counts required for the two material problem.**

hists./step	$\Delta t(sh)$	IMC (μs/hist.)	HOLO-ECMC (μs/hist)	Newton iters./LO Solve
100,000	0.001	17	3.5	4.9
30,000	0.001	18	6.9	5.0
30,000	0.005	59	7.4	7.6

1.3.4 Comparison of different HO Solvers

In this section we compare the results of our HOLO algorithm with different HO solvers for the test problems in Section 1.3.1 and 1.3.2. We compare standard MC (SMC) as a HO solver to the HOLO algorithm with ECMC using both three batches and a single batch, per time step. The use of a single batch is similar to the approach in [?]. Results are tabulated for 200 x cells, using the same total number of histories per time step, divided evenly among the batches.

Tables 1.6 and 1.7 compare the results for the Marshak wave and two material problems. The number of batches for each ECMC case is indicated in parenthesis. The FOM values are normalized to the reference IMC result for the corresponding problem. For HOLO-SMC there is minimal reduction in variance compared to IMC

in the Marshak wave problem, and the two material problem actually demonstrates worse variance. Sufficient histories are not performed to accurately estimate consistency terms throughout the problem. For ECMC, a single batch produces less variance than the case of three equal batches. This indicates that if the solution cannot be resolved with the trial space (i.e., the intensity is driven negative), a single large batch may be more accurate. It is noted that these results only account for statistical variance, and do not account for accuracy, which will depend on the estimates of ϵ computed each iteration.

Table 1.6: **Comparison of sample statistics for the Marshak Wave problem. Number of ECMC batches is indicated in parenthesis.**

	ß			FOM		
hists./step	SMC	ECMC (1)	ECMC (3)	SMC	ECMC (1)	ECMC (3)
12,000	2.77%	0.10%	0.28%	1.50	1280	145
100,000	0.98%	0.03%	0.06%	1.43	1270	422

Table 1.7: **Comparison of sample standard deviations for the two material problem. Number of ECMC batches is indicated in parenthesis.**

	ß			FOM		
hists./step	SMC	ECMC (1)	ECMC (3)	SMC	ECMC (1)	ECMC (3)
30,000	5.35%	0.002953%	0.011%	0.46	1.51×10^6	1.04×10^4
100,000	2.85%	0.001474%	0.0033%	0.49	1.80×10^6	3.59×10^4

1.3.5 Pre-heated Marshak wave problem and adaptive mesh refinement

Finally, to demonstrate the potential of ECMC with adaptive space-angle mesh refinement, we perform results for a modified Marshak wave problem. The problem is modified so that the LDFE trial space can accurately represent the solution (i.e., the intensity is strictly positive). Mesh refinement is of minimal use in the previous problems due to most of the error existing at the wavefronts, caused by the large cross sections. The modified problem has the same material properties and left boundary source as the Marshak wave problem in Section 1.3.1. However, the initial equilibrium temperature and right boundary condition are raised to 0.03 keV. The higher initial temperature reduces the initial cross section and increases the strength of the emission source within cells. The LDFE mesh can now sufficiently resolve the solution and lumping is not required by the LO solution. The simulation end time is 0.5 sh with a constant time step of $\Delta t = 0.001$ sh.

Fig. 1.4 compares the result from HOLO-ECMC with three batches and IMC. It was found that 100 x cells was sufficient to resolve the solution spatially. There is slightly more noise in IMC past the wavefront due to the increased emission source. Additionally, the opacity is thin enough that some photon energy is able to reach the right boundary, in front of the wavefront.

Table 1.8 compares the variances for this problem for the various HO solvers. The FOM values are normalized to the case of HOLO-SMC with 12,000 histories per time step. The final row of the table is for an ECMC simulation with adaptive mesh refinement (AMR). The strategy for refinement is described in Appendix **??**. The adaptive mesh refinement case used a total of nine batches, with a refinement occurring at the end of the third and sixth batches, for every time step. The initial number of histories was adjusted so that the average number of histories per time

21

step is near 100,000; on average 99,881 histories per time step were used. All ECMC meshes used 4 equally-spaced μ cells initially. The improvement in variance by ECMC compared to SMC is not as significant as for the other problems. This is a result of the reduced opacity leading to intensity changing throughout the spatial and angular domains. The FOM is highest for the case of ECMC with adaptive refinement. When the solution can be resolved, the adaptive algorithm allows for a higher convergence rate of statistical variance. It is noted that the consistency terms and LO solution are still computed over the fixed, coarser mesh. However, in general, the refined mesh can produce higher accuracy in consistency terms that is not being measured by the FOM.

Table 1.8: Comparison of sample statistics for the pre-heated marshak wave problem for 100 x cells. Number of ECMC batches is indicated in parenthesis.

	ß			FOM		
hists./step	SMC	ECMC (1)	ECMC (3)	SMC	ECMC (1)	ECMC (3)
12,000	0.86%	0.13%	0.24%	1	41	13
100,000	0.16%	0.042%	0.08%	3.32	52	15
99,881 (AMR, 9 batches)	–	0.038%		–	61	

1.4   Accuracy in the Equilibrium Diffusion Limit

A critical aspect for any numerical solution to the thermal radiative transfer equations is preservation of the equilibrium diffusion limit (EDL). We expect the LD representation in the LO equations to preserve the equilibrium diffusion limit. In this limit, the MC HO solution will estimate angular consistency terms associated with an isotropic intensity, based on a spatially LD emission source. Because the

spatial closure produces equations that are equivalent to an LDFE solution to the S_2 equations, we expect the equations to preserve the equilibrium diffusion limit [?, ?].

We test a problem in the EDL by adjusting material properties to produce a strongly diffusive region. The EDL problem has constant cross sections with $\sigma_a = 1000$ cm^{-1}, $\sigma_s = 10$ cm^{-1}, $\rho c_v = 6.8784 \times 10^{-3}$ Jk keV^{-1} cm^{-3}. The domain width is 0.1 cm and 4 μ cells and 3 batches of 4,000 histories are used for the single HO solve in all calculations. The simulation end time is 5 sh and a linear increase of 15% from $\Delta t = 0.001$ sh to a maximum $\Delta t = 0.01$ sh is used. We compare the LDFE LO solution to a LO solution using a step discretization, which is known to not preserve the EDL for S_N equations. The step discretization is implemented by using the scaled slope spatial closure in Sec. ?? with closure parameters $\gamma_i^\pm = 0$ for all cells.

The accuracy in the equilibrium diffusion limit is compared for thefthe two spatial discretizations, for different mesh sizes, in Fig. 1.5. As demonstrated, the LDFE spatial discretization has converged spatially, where both 20 and 200 cells produce the same location of the wave front. However, the step discretization artificially propagates the energy forward; the inaccuracy is greater than what would be expected from simply truncation error. The step discretization will only be accurate if the mesh cells are on the order of a mean free path, which is very large for this problem. Although not plotted, the material temperature overlays the radiation temperature for the LDFE solution, in equilibrium with the radiation.

1.5 CONCLUSIONS

We have been able to produce solutions for Marshak wave test problems using a new HOLO method that are in agreement with IMC. Unlike IMC, our method requires no effective scattering events to be included in the MC simulation, which

limits the run time of particle tracking, while adding the cost of a LO newton solver. Average LO iteration counts did not significantly increase as the time step size was increased. The LDFE spatial representation mitigates issues with teleportation error, producing results with spatial accuracy comparable to IMC with source tilting. The ECMC approach, with initial guesses based on the previous radiation intensity, results in efficient reduction of statistical error and allows for particles to be distributed to largely varying regions of the problem. The LO solver resolves the non-linearities in the equations resulting in a fully implicit time discretization. The LO solver can accurately and efficiently resolve the solution in diffusive regions, while the HO transport solver provides the accuracy of a full transport treatment where necessary.

The primary difficulty to overcome in the ECMC algorithm is when the solution cannot be accurately represented by the trial space, e.g., in optically thick cells where the solution is driven negative. We are currently developing an approach to allow the ECMC iterations to continue converging globally when there are such regions present. It is necessary to ensure the closure in the LO system is consistent with the HO representation for the solution in such regions. The ability to represent the solution accurately in rapidly varying regions of the problem will be key for generalization of this method to higher dimensions. A formulization of the ECMC method that allows for time-continuous MC transport (similar to IMC) is also currently being investigated. This may reduce some of the loss of accuracy in optically thin regions due to the time discretization of the transport equation in the HO solver. However, greater time accuracy is not of primary concern as this method is intended for use in problems dominated by large absorption opacities, where the LO acceleration is critical. Inclusion of Compton scattering in this algorithm, which would introduce additional non-linear dependence through energy exchange with the material, is a

topic for future research.

Future work will also explore the accuracy of the HOLO method, in particular, analyzing the optimal number of batches and the benefit of adaptive refinement. This will likely require the use of manufactured solutions. The sensitivity of the method to mesh sizes and time step sizes will be investigated more thoroughly. Ultimately, we plan to extend this method to multiple spatial dimensions for the case of multigroup TRT equations. For TRT problems, it is important that the LO spatial discretization satisfies the equilibirium diffusion limit. To extend to higher dimensions, our LDFE representation may require the use of a higher-degree spatial representation for the LO system to achieve the diffusion limit. Further asymptotic analysis on the method will be applied before implementation. It may be necessary to use a different LO system (e.g., the non-linear diffusion acceleration approach in [**?**]), if the S_2-like equations become too inefficient or difficult to implement in higher dimensions. Alternatively, a variable Eddington Tensor approach may provide more stability in rapidly variable regions of the problem while still allowing for a consistent, LDFE solution that is efficiently solvable.
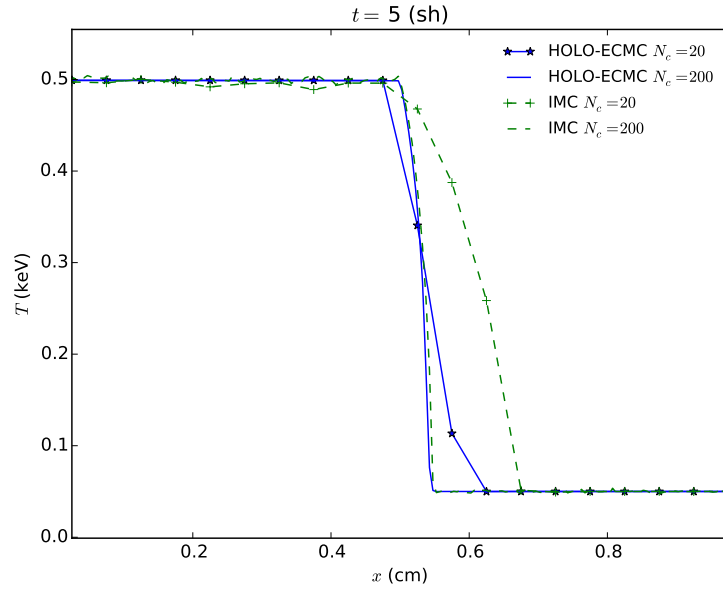
ACKNOWLEDGEMENTS
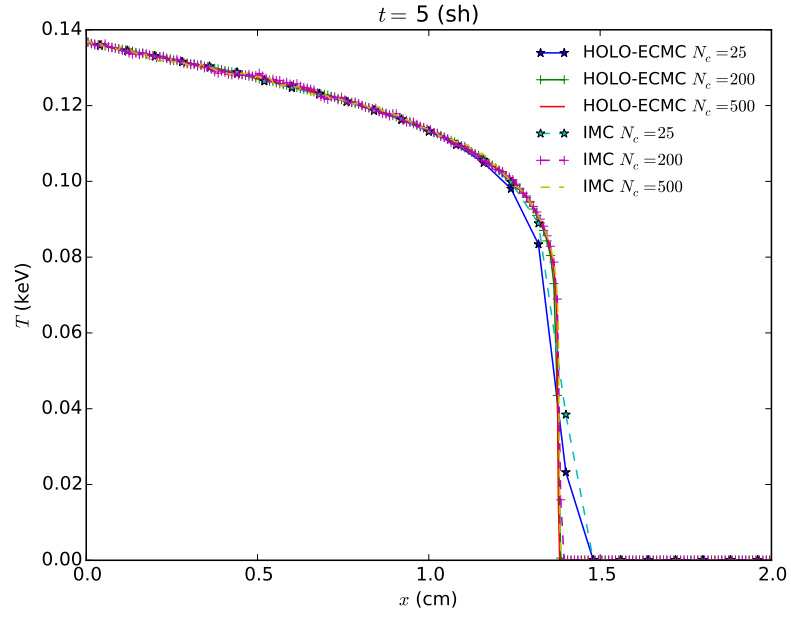
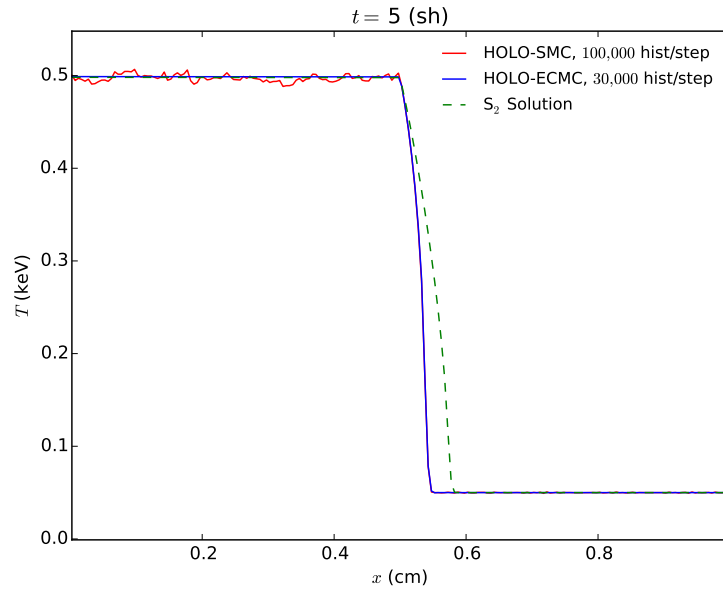(a) Convergence of IMC and HOLO-ECMC solutions.
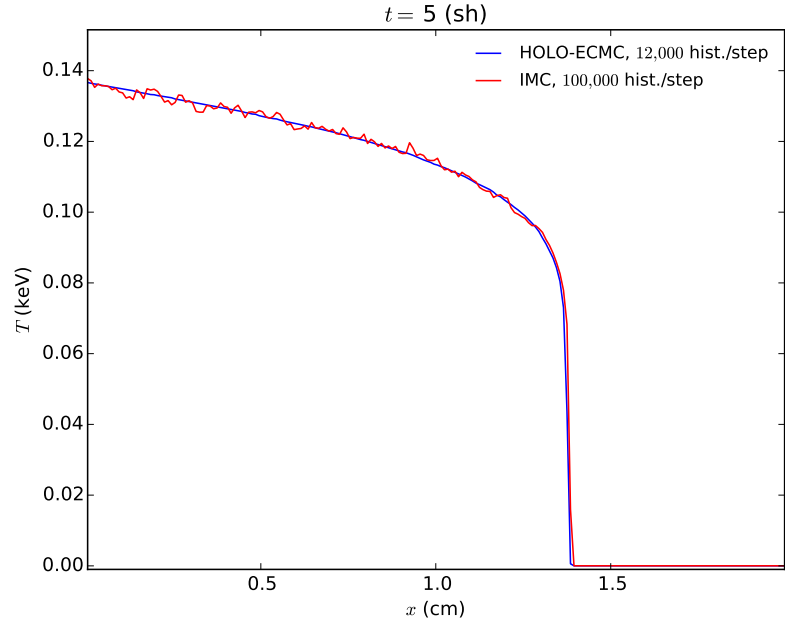
(b) Comparison of solutions for 200 spatial cells.

Figure 1.2: Comparison of radiation temperatures for Marshak wave problem at $t = 5$ sh.

(a) Comparison of IMC and HOLO-ECMC.

(b) Comparison of SMC and ECMC HO solvers.

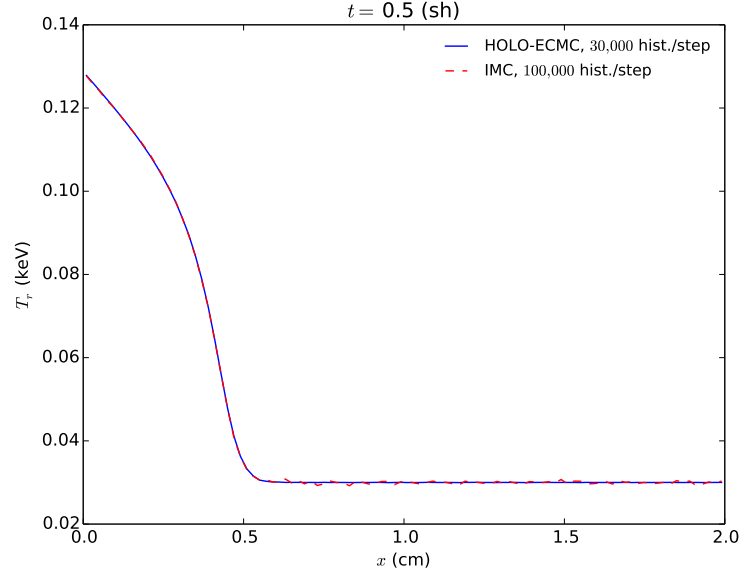Figure 1.3: **Comparison of radiation temperatures for two material problem.**

Figure 1.4: Comparison of radiation temperatures for the pre-heated Marshak wave problem for 100 x cells at **t = 0.5** sh.
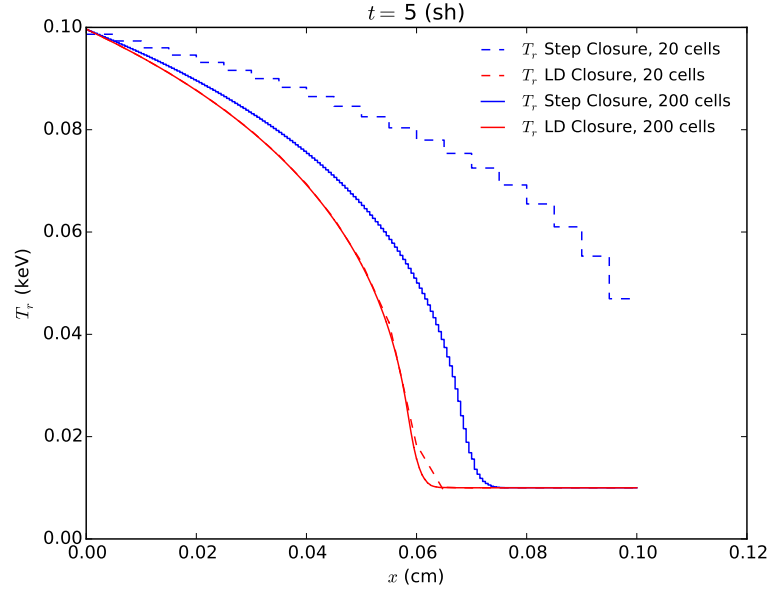

Figure 1.5: Comparison of T_r for step and LDFE discretizations of the LO equations in the equilibrium diffusion limit.

2. RESIDUAL MONTE CARLO TREATMENT OF THE TIME VARIABLE

Another extension and improvement for the HOLO method described in Sec. **??** is the time discretization of the transport equation. We have incorporated the time variable into the ECMC method to improve efficiency over IMC, while still preserving the accuracy of MC integration. The main area of interest is in producing more accurate resolution of radiation wave-fronts in optically thin regions, where particles transport a long distance over a time step. In such regions, the MC integration of the time variable by IMC can produce greater accuracy than an implicit Euler discretization, which can produce artificially fast propagation of radiation in space. A potential application where this accuracy is important is stellar atmosphere calculations. It is noted that no adaptive refinement in time is performed, so maintaining exponential convergence may not be possible. However, we still expect the residual MC formulation of the ECMC method to show improvement in efficiency over standard MC.

In the remainder of this chapter, the inclusion of the time variable into the ECMC trial space is detailed, along with modifications to particle tracking and the ECMC algorithm. The process of sampling, tracking, and tallies particle histories in time is detailed in literature[**?**, 1, **?**, **?**], but sufficient details are provided in this chapter. Finally, a new temporal closure for the LO equations is given, and results are compared to IMC for accuracy and efficiency.

2.1 Modifications to the HO equations

Inclusion of the time variable t in the trial space used by ECMC allows for no discretization of the transport operator $\mathbf{L}$. The transport operator, applied to the

continuous intensity I, becomes

$$\mathbf{L}I(x,\mu,t) = \frac{1}{c}\frac{\partial I}{\partial t} + \mu\frac{\partial I}{\partial x} + \sigma_t I \tag{2.1}$$

The emission source is still treated with an implicit Euler discretization, which is similar to the approximation made in IMC. The ECMC algorithm specified in Sec. **??** does not need to be modified. However, the residual source and trial-space representation are modified to include t. Each batch is still estimating the error in the current projection estimate $\tilde{I}(x,\mu,t)$, but the time variable must be included in the inversion of the $\mathbf{L}$ operator.

2.1.1   The Doubly-Discontinuous Trial Space in Time

It is necessary to define a new trial space that includes the time variable so that we can explicitly evaluate the residual. The time variable has a similar representation to the LDD trial space used for the spatial variable in Sec. **??**, but the solution is a constant value over the interior of the time step. This step, doubly-discontinuous (SDD) trial space is defined as

$$\tilde{I}(x,\mu,t) = \begin{cases} \tilde{I}^n(x,\mu) & t = t^n \\ \overline{I}(x,\mu) & t \in (t^n, t^{n+1}) \\ \tilde{I}^{n+1}(x,\mu) & t = t^{n+1} \end{cases} \tag{2.2}$$

where we have used $\overline{I}$ to denote the time-averaged LDFE *projection* in x and μ of the intensity over the interior of the time step; the beginning and end of time step projections are denoted $\tilde{I}^n$ and $\tilde{I}^{n+1}$, respectively. An illustration of t for the SDD trial space, over the n-th time step, is depicted in Fig. 2.1. There is a projection error in using the LDFE projection to represent the intensity between time steps. However,

with sufficient noise reduction and mesh resolution, this should be an acceptable error compared to the large statistical noise of standard MC.
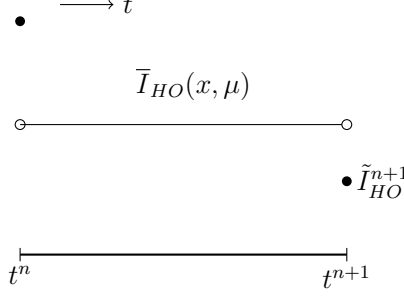

Figure 2.1: Step doubly-discontinuous representation of t for the HO solution.

The SDD trial space provides a projection for all the desired unknowns to exactly produce the moment equations, i.e., the time-averaged, end of time step, and previous time step intensities; temporally, these are the only unknowns that appear in equations that have been integrated over a time step to produce a balance statement. Another benefit of this trial space is it allows for infrastructure for computing the residual from the time-discrete case to be used directly. This trial space has one major drawback: only particle histories that reach t^{n+1} contribute to the estimation of $\tilde{\epsilon}^{n+1}$, and thus I^{n+1}. This is undesirable in optically thick problems.

REWRITE: Possibly move this to the future work section Alternatively, an LDFE representation could be used in the time variable. The linear representation would produce less noise because all particle tracks contribute to the slope, rather than just those that reach the end of the time step, although it would produce an approximate projection error for the end of time step intensity that is not produced with a discontinuity at the end of the time step. The linear representation in time would also

31

produce a more accurate reconstruction of the scattering source in time. However, a linear representation requires the sampling algorithm to be significantly modified because the L_1 integral for computing the residual magnitude is now significantly complicated by the tri-linear function. A possible way to sample this source is discussed in Appendix??? for completeness, but it has not been rigorously investigated.

2.1.2 Residual Source Definition and Sampling

The residual is defined as $r = q - \mathbf{L}\tilde{I}(x, \mu, t)$, where

$$q = \left(\sigma_a ac(T_{LO}^{n+1})^4(x) + \sigma_s \overline{\phi}_{LO}\right) \tag{2.3}$$

is a constant in time and provided by the LO solver. We have assumed a constant reconstruction for the scattering source in time. Evaluation of the residual with Eq. (2.2) for I produces a uniform source in time, as well as a δ-function source at the beginning and end of the time step. We write the residual source in terms of three components:

$$r(x, \mu, t) = \overline{r}(x, \mu) + r^n(x, \mu)\delta^+(t - t^n) + r^{n+1}(x, \mu)\delta^-(t - t^{n+1}), \quad t \in [t^n, t^{n+1}] \tag{2.4}$$

We will look at each component individually. The first residual term is a constant in time with representation

$$\overline{r}(x, \mu) = q - \mu\frac{\partial \overline{I}(x, \mu)}{\partial x} - \sigma_t \overline{I}(x, \mu) \tag{2.5}$$

Evaluation of the above function produces both face and volumetric sources, similar to in the discrete case. To sample x and μ from the face and volume distributions, the same rejection procedure can be used as for Eq. (??) and detailed in [3]. The

time variable can then be sampled uniformly over the time step, i.e., $t = t^n + \eta \Delta t$, where η is a uniform random variable with support $(0, 1)$.

The second source has definition

$$r^n(x, \mu) = -\frac{1}{c} \frac{\partial \overline{I}(x, \mu)}{\partial t}\bigg|_{t=t^n} = -\frac{1}{c}\left(\overline{I}(x, \mu) - \tilde{I}^n(x, \mu)\right) \qquad (2.6)$$

This source is a LDFE space and angle volumetric source. The rejection sampling procedure is used to sample x and μ. All particles sampled from this source begin tracking with $t = t^n$.

The final source term is

$$r^{n+1}(x, \mu) = -\frac{1}{c} \frac{\partial \overline{I}(x, \mu)}{\partial t}\bigg|_{t=t^{n+1}} = -\frac{1}{c}\left(\tilde{I}^{n+1}(x, \mu) - \overline{I}(x, \mu)\right). \qquad (2.7)$$

The source r^{n+1} can be treated using the same analytic treatment as the outflow face source in the LDD trial space, detailed in Sec. **??**; the source at the end of the time step is never sampled because its contribution to I^{n+1} can be analytically computed. To treat the sources this way, the solution for $\tilde{I}^{n+1}(x, \mu)$ is initialized to the value of $\overline{I}(x, \mu)$ before a batch of particles begins. Then, error particles that reach the end of the time step, referred to as "census" particles, contribute a standard score to the projection $\tilde{I}^{n+1}(x, \mu)$.

With these definitions, it is thus only necessary to sample from two sources. Using composite-rejection sampling [4], a discrete probability distribution is sampled to determine which source component to sample, followed by sampling of that component. The algorithm is

1. Sample uniform random number η

2. If $\eta < \|r^n\|_1 / (\|r^n\|_1 + \|r^{n+1}\|_1)$:

- Sample from r^n source using rejection sampling

- Sample t uniformly over (t^n, t^{n+1}).

3. Else:

- Sample from $\bar{r}$ source

All L_1 integrals can be analytically integrated using the same numerics as in the time-discrete case. The systematic sampling algorithm, as described in Sec. **??**, can be applied similarly. However, the choice of source is only make locally over that space-angle element. In that case, the element is chosen systematically, then the choice of r^n or $\bar{r}$ is sampled. REWRITE: Only discuss sampling of systematic case.

2.1.3   Importance Sampling on Interior of Time Step

As an attempt to reduce variance in the estimate of $\tilde{\epsilon}^{n+1}(x, \mu)$, we use important sampling in the time variable. Systematic sampling is still used for determining the cell of interest, and sampling as described above is used to determine which source is sampled, based on the appropriate probabilities described in the previous section. However, when the interior source $\bar{r}(x, \mu)$ is sampled, we use importance sampling for the conditional sampling of the uniform time step. The goal is to ensure that some histories reach the end of the time step. In order to do this, we sample from a modified PDF such that a fraction p_{end} of particles sampled from $\bar{r}(x, \mu)$ are born with $t \in (t^{end}, t^{n+1})$. We define $t^{end} = t^{n+1} - M/(c\sigma_t)$, where M is the desired number of MFP of travel the particle will undergo from the end of the time step (e.g., 2 or 3). The weights of particles sampled from this distribution must be modified to prevent source biasing.

The new PDF to be sampled from is

$$f^*(t) = \begin{cases} \dfrac{1 - p_{end}}{t^{end} - t^n} & 0 < t < t^{end} \\ \dfrac{p_{end}}{t^{n+1} - t^{end}} & t^{end} \leq t < t^{n+1} \\ 0 & \text{elsewhere} \end{cases} \tag{2.8}$$

The original PDF is $f(t) = 1/\Delta t$, for $t \in (t^n, t^{n+1})$. Thus, using the standard procedure for importance sampling[4], the starting time t_{start} is sampled from $f^*(t)$, and then weights are multiplied by the factor $f(t_{\text{start}})/f^*(t_{\text{start}})$. This procedure is not perfect in that if a particle is moving from an optically thin to an optically thick region, it is not guaranteed to reach census. However, this case does not introduce bias.

2.1.4   Tracking and Tallying in Time

Because our LO equations will be integrated over the time step, we only need to perform MC tracking for $t \in [t^n, t^{n+1}]$. The initial time for the particle is sampled as described in the previous section. In inverting the **L** operator, particles are tracked until they reach the end of the time step. Path lengths are sampled or the weight is exponentially attenuated as before (e.g., Sec. **??**). As a particle travels from position x_o to x_f, with direction μ, the time is updated as

$$t^f = t^0 + \frac{|x_f - x_o|}{c\mu} \tag{2.9}$$

where c is the speed of light. For analog path-length sampling, if $t^f > t^{n+1}$ then t^f is adjusted to t^{n+1} and the path length is adjusted accordingly. For continuous weight deposition, particles are only tracked until they reach t^{n+1}. A proof that this process of tracking particles is a MC solution to an integral equation that is exactly inverse

to the **L** operator is detailed in [?, ?].

Tallies must be adjusted to account for the averaging over the time step, and to compute the intensity at the end of time step. To produced the time-averaged representation $\overline{I}(x, \mu)$, requires estimators for the average, x, and μ moments of the error, e.g.,

$$\overline{\epsilon}_{x,ij} = \frac{1}{\Delta t} \frac{6}{h_j} \int\limits_{t^n}^{t^{n+1}} \mathrm{d}t \int\limits_{x_{i-1/2}}^{x_{i+1/2}} \mathrm{d}x \int\limits_{\mu_{j-1/2}}^{\mu_{j+1/2}} \mathrm{d}\mu \left(\frac{x - x_j}{h_i}\right) \epsilon(x, \mu, t) \tag{2.10}$$

with a similar definition for the average and μ moments. The estimators are defined as

$$\hat{\overline{\epsilon}}_{x,ij} = \frac{1}{N_{hist}} \frac{6}{\Delta t h_i} \sum_{n=1}^{N_{hist}} \frac{s_n}{h_i h_j} w_j \left(x_c - x_i\right), \tag{2.11}$$

where the magnitude of the weights produce the L_1 integral over all phase space, i.e.,

$$\sum_{n=1}^{N} w_n = \|r(x, \mu, t)\|_1 \equiv \int\limits_{t^n}^{t^{n+1}} \mathrm{d}t \int\limits_{x_{i-1/2}}^{x_{i+1/2}} \mathrm{d}x \int\limits_{\mu_{j-1/2}}^{\mu_{j+1/2}} \mathrm{d}\mu \, |r(x, \mu, t)|. \tag{2.12}$$

Here, x_c is the center of the n-th path length, and s_n is the path length for the n-th path length in the $x - \mu$ cell.

Moments of $I^{n+1}(x, \mu)$ must be estimated to represent the end of time step intensity. For example, the x moment for the ij-th cell of the error at the end of time step is

$$\epsilon_{x,ij}^{n+1} = \frac{6}{h_i} \iint\limits_{\mathcal{D}_{ij}} \left(\frac{x - x_i}{h_i}\right) \epsilon(x, \mu, t^{n+1}) \mathrm{d}x \mathrm{d}\mu \tag{2.13}$$

The estimators for these moments are a generalization of the census tallies used in IMC [?, ?]. The tallies are based on the definition of the intensity as $I(x, \mu, t) = ch\nu N(x, \mu, t)$ given in Eq. (??), similar to collision estimators [4, ?]. The census

36

estimator for the x moment is

$$\hat{\epsilon}_{x,ij}^{n+1} = \frac{1}{N_{hist}} \frac{6}{h_j h_i} \sum_{n=1}^{N_{hist}} c w_j \left(x_c - x_i\right) \qquad (2.14)$$

Similar tallies are defined for the other space-angle moments. These tallies can be exceptionally noisy because only particles that reach the end of the time step contribute.

2.2 Closing the LO Equations in Time

The LO equations must be closed in time consistently with the HO equations. Previous work has enforced consistency in time by adding a local artificial source to the time-discretized LO equations in each cell [7]. This source was approximated based on the difference between the exact HO integral of the time derivative and the approximate representation in the LO equations. The advantage of this form is that the LO solver exclusively deals in time-averaged unknowns for the radiation terms in the equations. However, if the problem is strongly non-linear or the time-averaged and time-edge values differ greatly, this may become unstable.

We will alternatively use a parametric closure in the time variable, similar to the spatial closures discussed in the Sec. **??**. The time-integrated LO equations can be written exclusively in terms of time-averaged unknowns. This closure produces LO equations that have the same numerical difficulty to solve as the BE, fully-discrete LO equations, but have the potential to preserve the accuracy of the MC integration in time, upon non-linear convergence of the system. A closure relation is used to eliminate the end of time step moments present from the time derivative term. We will investigate different parametric forms of the closure for robustness. Once the time-averaged unknowns have been calculated, the time closures can be used to convert the time-averaged unknowns to end-of-time-step values.

REWRITE THIS SENTENCE One potential benefit of the time closure parameters is that $\overline{I}^{HO}$ will be most different from $I^{HO,n+1}$ in problems that are optically thin. In such problems, σ_a is small, leading to an optically thin problem. However, there may be difficulties in the MPV problems where the problems are tightly coupled and nonlinear, but can lead to a large change over a time step.

REWRITE: I think most of these paragraphs can be moved to intro

2.2.1   Derivation of Time-Averaged Moment Equations

The time-continuous radiation equations are integrated in space and angle the same as before. For example, the L and $+$ moment equation is

$$\frac{1}{c}\frac{\partial}{\partial t}\langle\phi\rangle^+_L - 2\left(\mu_{i-1/2}I_{i-1/2}\right)^+ + \langle\mu I\rangle^+_{L,i} + \langle\mu I\rangle^+_{R,i} + \sigma_{t,i}h_i\langle\phi\rangle^+_{L,i} - \frac{\sigma_{s,i}h_i}{2}\left(\langle\phi\rangle^+_{L,i} + \langle\phi\rangle^-_{L,i}\right)$$
$$= \frac{h_i}{2}\langle\sigma_a acT^4\rangle_{L,i} \quad (2.15)$$

This equation is then integrated over the time step, and the emission source is assumed implicit. The same manipulations can be performed on the streaming term to form angular consistency terms, but the weighting fluxes are now time-averaged values. Thus, the angular consistency terms are computed with $\overline{I}(x,\mu)$. The equations with time-averaged consistency terms are

$$\frac{\langle\phi\rangle^{+,n+1}_{L,i} - \langle\phi\rangle^{+,n}_{L,i}}{c\Delta t} - 2\overline{\mu}^+_{i-1/2}\overline{\phi}^+_{i-1/2} + \overline{\{\mu\}}^+_{L,i}\langle\overline{\phi}\rangle^+_{L,i} + \overline{\{\mu\}}^+_{R,i}\langle\overline{\phi}\rangle^+_{R,i} + \sigma^{n+1}_{t,i}h_i\langle\overline{\phi}\rangle^{n+1,+}_{L,i}$$
$$- \frac{\sigma_{s,i}h_i}{2}\left(\langle\overline{\phi}\rangle^+_{L,i} + \langle\overline{\phi}\rangle^-_{L,i}\right) = \frac{h_i}{2}\langle\sigma^{n+1}_a acT^{n+1,4}\rangle_{L,i}, \quad (2.16)$$

These equations are exact at this point. The BE approximation is used for the temperature terms in the material energy equations, but the radiation energy deposition is a time-averaged valued. REWRITE: Maybe add material energy equation

38

2.2.2 Parametric Time Closure

The closure relations in time are different than the closure relations for the spatial variable because we do not have a slope in time. The following closure is a modified diamond relation:

$$I^{n+1} = 2\gamma \overline{I} - I^n \qquad (2.17)$$

where γ is the closure factor and $\overline{I}$ is the time-averaged intensity. A modified BE discretization can also be used:

$$I^{n+1} = \gamma \overline{I} \qquad (2.18)$$

The chosen closure relation must be used to eliminate the unknowns at t^{n+1} from each of the LO moment equations, with the values from the previous time step taken as a known quantity. Thus, it is necessary to have a closure relation for each moment and half range, producing four closure parameters per spatial cell. The closure relations for the L moment and the modified diamond relation are

$$\langle \phi \rangle_{L,i}^{\pm,n+1} = 2\gamma_{L,i}^{\pm} \langle \overline{\phi} \rangle_{L,i}^{\pm} - \langle \phi \rangle_{L,i}^{\pm,n} \qquad (2.19)$$

with equivalent definitions for the R moment. Substitution of the above equation into Eq. (2.16)

$$\frac{2}{c\Delta t} \left[\gamma_{L,i}^{+} \langle \phi \rangle_{L}^{+,n+1} - \langle \phi \rangle_{L}^{+,n} \right] - 2\overline{\mu}_{i-1/2}^{+} \overline{\phi}_{i-1/2}^{+} + \overline{\{\mu\}}_{L,i}^{+} \langle \overline{\phi} \rangle_{L,i}^{+} + \overline{\{\mu\}}_{R,i}^{+} \langle \overline{\phi} \rangle_{R,i}^{+} + \sigma_{t,i}^{n+1} h_i \langle \overline{\phi} \rangle_{L,i}^{n+1,+}$$
$$- \frac{\sigma_{s,i} h_i}{2} \left(\langle \overline{\phi} \rangle_{L,i}^{+} + \langle \overline{\phi} \rangle_{L,i}^{-} \right) = \frac{h_i}{2} \langle \sigma_a^{n+1} acT^{n+1,4} \rangle_{L,i}, \quad (2.20)$$

The other moment equations are analogously defined.

The value of $\gamma_{L,i}^{+}$, $\gamma_{R,i}^{+}$, $\gamma_{L,i}^{-}$, and $\gamma_{R,i}^{-}$ can be computed by substituting the trial-space representation of $I^{HO}(x,\mu,t)$ into Eq. (2.19) and its analogs.

2.3 Computational Results

We will test the time-closure in several characteristic cases. Throughout this section the Backward Euler discretized results are indicated with HOLO-BE and the MC-based time closure are indicated with HOLO-TC, where applicable. The first case is a near-void where the time-closure parameters will provide the most correction compared to a Backward Euler discretization. The second problem is the Marshak wave problem from Sec. **??**. This problem is optically thick, so minimal time-correction is needed, but there will likely be higher variance in the census tallies. We will compare to IMC visually for accuracy to determine that we are converging towards the correct solution. For the near void case the IMC solution is accurate because the material energy equation is uncoupled. The systematic sampling algorithm detailed in Sec. **??** was used for all HOLO results in this section.

2.3.1 Near-Void Problem

The material properties are uniform throughout the 2.0 cm domain with $\rho c_v = 0.01374$ Jks cm^{-3} keV^{-1}, $\sigma_a = 10^{-6}$ cm^{-1}, and $\sigma_s = 0$ cm^{-1}. The material and radiation are initially in equilibrium at a temperature of 0.01 keV. An isotropic incident intensity of 0.150 keV is applied at $x = 0$; the incident intensity on the right boundary is 0.01 keV. The simulation end time is 0.003 sh. Because the problem is optically thin, no importance sampling on the interior of the time step is used.
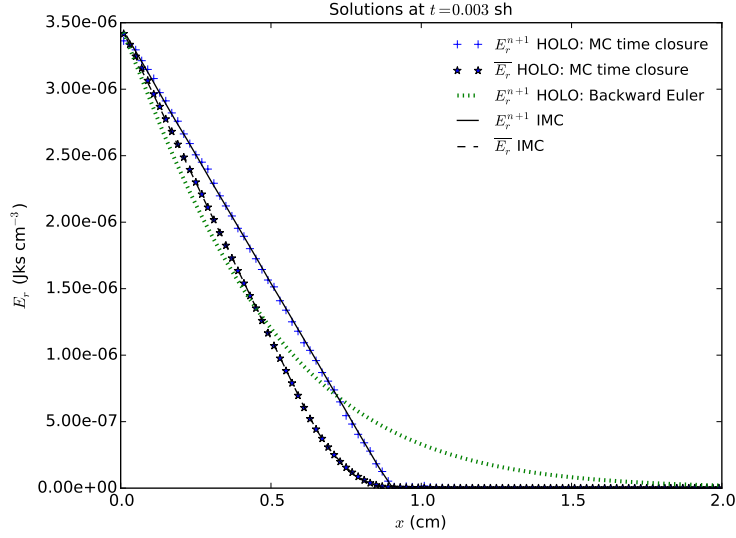
Figure 2.2: Comparison of radiation energy densities of IMC and HOLO method for the HO time closure and a BE discretization.

A comparison of the cell-averaged radiation energy densities E_r for IMC and the HOLO method with the diamond-like HO time closure are depicted in Fig. **??**, both for the time-averaged solutions and end-of time step values in the final time step. The end of time step values for the HOLO method with a BE discretization is also depicted. For the HOLO results, three ECMC batches were performed with a total of 3×10^6 histories per time step and the IMC results were generated with 12×10^6 histories per time step. The spatial mesh had 100 spatial cells and the ECMC results used 40 μ cells. The MC treatment of the time variable and the closure of the LO equations allow the results to correctly reconstruct the wave-front of IMC. There is some dispersion at the wave front presented in the 1 batch case that results from projection onto the spatial mesh at the foot of the wave.

Figure. 2.4 compares radiation energy densities for various numbers of μ cells. At coarser mesh sizes, the imprinting of the mesh is visible in the location of the

wave-front. This is a result of the projection onto the space-angle mesh between time steps. As the mesh is refined, the solution coverges towards the IMC solution. It is noted that the results are equivalent for either the diamond-like or implicit-like closures in this problem. This is because the problem is nearly linear as the material is uncoupled from the radiation.
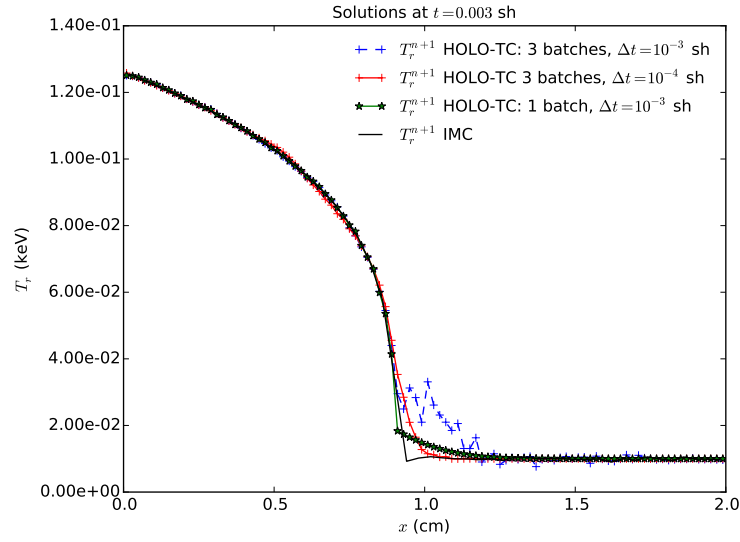

Figure 2.3: Comparison of radiation temperatures for the HOLO method for different time step and batch sizes.
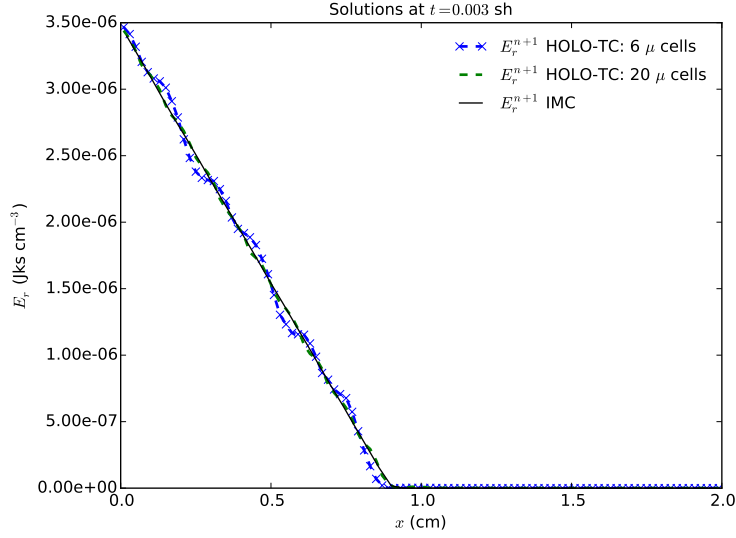
Figure 2.4: Comparison of radiation energy densities for the HOLO method with different numbers of μ cells. $\Delta t = 0.001$ sh

The census radiation temperatures determined with the HOLO method are plotted in Fig. 2.3 for two different time step sizes and a case with . By plotting proportional to the fourth-root of the radiation energy density, the noise at low magnitudes past the wave-front are more apparent. This noise is small in comparison to the overall scale of the radiation energy density, but it results from particles being born near the wave-front with a time sampled near the beginning of the time step. Negativities can occur out front of the wave. In the algorithm the average is set to the floor value and slopes to zero in such cells. At the smaller time steps, the noise is less visible because there is less inaccuracy in the step approximation over the interior of the time step. These inaccuracies should be reduced by the linear time trial space. Causality is not strictly preserved because you are sampling the error, so it is possible to have particles reach the front of the wave front. This is not a bias, just insufficient sampling.

A comparsion for radiation temperatures with 1 and 3 batches is given in Fig. **??**, which reveals that there is substantial noise past the wave front for the 3 batches case. This noise is small relative to the scale of the solution in the wave-front, which is why it is not visible in the mean intensity plots. This demonstrates one deficiency in this methdo that particles sampled near the wave-front can potentially ahve a time near the beginning of the time step and travel into the equilibrium region. The solution is not biased however, if sufficient samplign was performed there woudl be negative particles that canceled out this error. The residual MC case does not display this error as drastically because the guessed solution takes on the form of the old solution, particles can not transport past what physics allows, with the exception of some smearing due to the projection error incurred between time steps.

We have computed FOM statistics using Eq. (1.26) with 20 independent runs for each problem set up and parameters. The different number of batches for the HOLO methods are indicated in parenthesis next to the algorithm.

Table 2.1: **Comparison of sample statistics for the Near-Void problem. Simulation end time is t = 0.003 sh.**

	ß		FOM	
hists./step	IMC	HOLO-ECMC	IMC	HOLO-ECMC
300,000 1,000,000	3.40%	0.28%	1	145
2,000,000	1.22%	0.057%	0.93	422

REFERENCES

[1] J. A. Fleck, Jr. and J. D. Cummings, Jr. An implicit monte carlo scheme for calculating time and frequency dependent nonlinear radiation transport. *J. Comput. Phys.*, 8(3):313–342, December 1971.

[2] Elmer Eugene Lewis and Warren F Miller. *Computational methods of neutron transport.* John Wiley and Sons, Inc., New York, NY, 1984.

[3] J.R. Peterson. Exponentially Convergent Monte Carlo for the 1-d Transport Equation. Master's thesis, Texas A&M, 2014.

[4] J.K. Shultis and W.L. Dunn. *Exploring Monte Carlo Methods.* Academic Press, Burlington, MA 01803, 2012.

[5] "Weston M. Stacey". *"Nuclear Reactor Physics".* Wiley, 2007.

[6] T.A. Wareing. *Asymptotic diffusion accelerated discontinuous finite element methods for transport problems.* PhD thesis, Michigan, 1991.

[7] Allan B. Wollaber, H. Park, R.B. Lowrie, R.M. Rauenzahn, and M.E. Cleveland. Radiation hydrodynamics with a high-order, low-order method. In *ANS Topical Meeting, International Topical Meeting on Mathematics and Computation,* Nashville Tennessee, 2015.